On the Structure of the Near Field of Oxy-Fuel Jet Flames Using Raman/Rayleigh Laser Diagnostics

Alexis Sevault[a], Matthew Dunn[b], Robert S. Barlow[b] and Mario Ditaranto[c]

[a]Energy and Process Engineering Department, Norwegian University of Science & Technology, 7491 Trondheim, Norway.
Corresponding author: E-mail: Alexis.Sevault@ntnu.no, Tel: +47 735 93 089.

[b]Combustion Research Facility, Sandia National Laboratories, Livermore, CA 94551-0969, USA.
E-mails: Barlow@sandia.gov, matthew.dunn@sydney.edu.au.

[c]Department of Energy Processes, SINTEF Energy Research, 7465 Trondheim, Norway.
E-mail: Mario.Ditaranto@sintef.no.

Abstract

An experimental study on turbulent non-premixed jet flames is presented with focus on CO_2-diluted oxy-fuel combustion using a coflow burner. Measurements of local temperatures and concentrations of the main species CO_2, O_2, CO, N_2, CH_4, H_2O and H_2 were achieved using the simultaneous line-imaged Raman/Rayleigh laser diagnostics setup at Sandia National Laboratories. Two series of flames burning mixtures of methane and hydrogen were investigated. In the first series, the hydrogen molar fraction in the fuel was varied from 37 to 55 %, with a constant jet exit Reynolds number Re_{Fuel} of 15,000. In the second series the jet exit Reynolds number was varied from 12,000 to 18,000, while keeping 55 % H_2 molar fraction in the fuel. Besides local temperatures and concentrations, the results revealed insights on the behaviour of localized extinction in the near-field. It was observed that the degree of extinction increased as the hydrogen content in fuel was decreased and as the jet Reynolds number was increased. Based on the distribution of the temperature, a fully burning probability index able to quantify the degree of extinction along the streamwise coordinate was defined and applied to the present flame measurements. A comparison of measured conditional mean of mass fractions and laminar flame calculations underlined the significant level of differential diffusion in the near-field that tended to decrease farther downstream. The results also showed high local CO levels induced by the high content of CO_2 in the oxidizer and flame products. A shift of maximum flame temperature was observed toward the rich side of the mixture fraction space, most likely as a consequence of reduced heat release in the presence of product dissociation. Main characteristics of laser Raman scattering measurements in CO_2-diluted oxy-fuel conditions compared to air-diluted conditions are also highlighted. Most data, including scalar fluctuations and conditional statistics are available upon request.

Keywords

Oxy-fuel, jet flame, CO_2-diluted, localized extinction, Raman, differential diffusion.

1.   Introduction

Due to climate change and favourable policies aiming at reducing carbon dioxide emissions, carbon capture and storage (CCS) technologies are seen as an effective panel of solutions for a transition between today's mostly combustion-based energy production, generating undesirable emissions, and tomorrow's energy production mostly based on renewables. Based on the great advance in oxygen separation technologies, which leads to reduced costs and the absence of post-combustion constraints, oxy-fuel combustion stands for a potentially efficient solution among the available CCS processes. Bolland et al. [1, 2] and Tan et al. [3] studied the design of oxy-fuel gas turbines fired with natural gas as a CO_2 removal option. The authors concluded that using partial flue gas recirculation offers a great potential for short-term feasibility and provides better operating conditions for the CO_2 scrubber performance compared to a plant equipped with a CO_2 scrubber without recirculation. Using O_2/CO_2 mixtures instead of air for fuel combustion ideally results in exhaust gases composed of water, which can be easily separated by condensation, and relatively pure carbon dioxide that can be captured, used in the semi-closed power cycle, and stored.
An advantage of this technology is its potential to reduce nitric oxides (NO_x) emissions. Ditaranto et al. [4-6] investigated NO_x emissions from oxy-fuel flames without CO_2 dilution, as it is used in glass melting industry for instance. The authors observed that NO_x emissions are especially influenced by air leaks and residual N_2 present in either natural gas or oxygen stream. Indeed, small amounts of N_2 can lead to significant NO_x emissions due to the high-temperature characteristic of oxy-fuel flames and the induced predominance of the thermal mechanism. However, if CO_2 dilution is considered, flame temperatures can be significantly reduced and NO_x emissions are expected to be lower than in air-diluted conditions [7].

The heat transfer properties of CO_2 are radically different from those of N_2. Consequently, as Ditaranto et al. [8] observed, CO_2 molecules radiate much more than N_2 molecules and tend to locally quench the chemical reaction. It has been seen in different studies [8, 9] that the molar percentage of oxygen in the oxidant should be around 30 % to reach air flame like stability, depending on the mixing process. In the present study, the oxygen molar fraction is set to 32 % in the oxidizer mixture. It has been observed that turbulent jet flames barely sustain with less than 30 % oxygen using a coflow burner. However, optimizing the mixing enables to stabilize turbulent flames with lower oxygen content in the oxidizer. For instance, Kutne et al. [10] stabilized oxy-fuel flames with contents as low as 20 % oxygen in the oxidizer by using swirl and partial premixing. The choice of using a coflow in the present study has been motivated by the interest in observing how the turbulent mixing is characterized in CO_2-diluted oxy-fuel flames.

Another phenomenon that may affect the flame structure is differential diffusion, which is especially likely to happen with high H_2 content in the fuel, though its magnitude in jet flames may progressively decrease as the Reynolds number and streamwise distance increase [11-13]. Computational codes do not necessarily take differential diffusion into account since they are most likely industry-oriented, where Reynolds numbers are much higher than at laboratory scale. Since one purpose of the present experiments is to provide data for validation of computational codes, the Reynolds numbers have been set to the highest achievable values in the laboratory conditions to minimize the effect of this phenomenon.

Besides limiting the flames series to stabilized conditions on a simple jet burner, laser Raman/Rayleigh scattering technique restricted the study to non-sooting flames, at least over most of their length. Indeed, hydrocarbon fluorescence from fuel-rich zones, where soot is likely to form locally, considerably affects Raman signals. The local soot level is very sensitive to the oxygen content in the oxidizer, as observed in previous studies on combustion in oxygen-enriched oxidizers [14, 15]. In the present case, due to the high H_2 content in the fuel, the level of fluorescence interferences coming from soot formation was at an acceptable level so that the Raman and Rayleigh signals could be confidently corrected.

2.   Specific Objectives

Literature regarding CO_2-diluted oxy-fuel flame structure and composition is scarce. The objectives of this study were to investigate the detailed scalar structure of CO_2-diluted oxy-fuel jet flames, exhibiting strong effects of turbulence chemistry interaction, and thereby provide new insights and data that may be used for improvement or validation of combustion models. Another purpose was to highlight the main particularities of using laser Raman scattering technique in CO_2-diluted oxy-fuel flames compared to air-diluted conditions.

Five flames were investigated in order to parametrically determine the effects of fuel composition (CH_4/H_2 molar fraction) and jet exit Reynolds number on the degree of localized extinction measured in the flame. Localized extinctions have been recently studied by Barlow et al. [16] in piloted jet flames of CH_4/H_2/air, in comparable conditions. Accurate prediction of localized extinction is recognized as an important test of turbulent combustion models [17].

Two series of three flames were investigated (one flame is common to both series). Both series had a molar percentage of O_2 in the oxidizer of 32 %, based on volumetric flow rates of the fuel and the CO_2/O_2 coflow. In the A-series, the molar percentage of H_2 in the fuel was varied from 37 to 55 % with a constant jet Reynolds number Re_{Fuel} = 15,000. In the B-series, Re_{Fuel} was varied from 12,000 to 18,000 with a molar content of 55 % H_2 in the fuel. The coflow temperature was kept at 294 K for each flame. Details are shown in Table 1.

Table 1. CO_2-diluted oxy-fuel jet flames properties.

Name	$\%_{mol} H_2$ in fuel	Re_{Fuel}	Jet speed (m/s)	Coflow speed (m/s)	Stoichiometric mixture fraction	Adiabatic temperature at stoichiometry (K)
A-1	55	15,000	98.2	0.778	0.0535	2250
A-2	45	15,000	84.5	0.755	0.0553	2243
A-3	37	15,000	75.8	0.739	0.0565	2236
B-1	55	12,000	78.6	0.622	0.0535	2250
B-2	55	15,000	98.2	0.778	0.0535	2250
B-3	55	18,000	117.8	0.933	0.0535	2250

3.   Experimental Setup

Measurements were performed using the simultaneous line imaging of Raman/Rayleigh scattering developed at Sandia National Laboratories. Details of the hardware configuration can be found in [18]. The setup enabled measurements of single-shot profiles of temperature and the mass fractions of all major species (CO_2, O_2, CO, N_2, CH_4, H_2O and H_2). The spatial resolution was 0.104 mm along a ~6 mm section of the focused beam. The total energy in the test section for the Raman/Rayleigh measurements was 1 J/pulse at 532 nm with an overall pulse duration of ~400 ns obtained from combining three frequency-doubled Nd:YAG laser pulses. Due to the high level of radiation emitted by CO_2 within the flames, heat-sensitive devices close to the flame were protected by reflective aluminium foil. The large collection lens in front of the Raman/Rayleigh setup was shielded by a 150-mm square, 1-mm thick window of infrared absorbing filter glass (Schott KG2).

The fuel nozzle was 5-mm inside diameter with 0.5 mm wall thickness and squared-off end, which helped to stabilize attached flames. The fuel nozzle was surrounded by a laminar coflow of 96.5 mm inside diameter. Thanks to the H_2 content in the fuel, the flame remained attached to the fuel nozzle. The nozzle had its tip 40 mm above the coflow and was long enough so that when the fuel mixture reached the nozzle tip the flow was considered fully developed. The oxidizer mixture first flowed through a series of perforated plates and then through a honeycomb to allow a uniform flow distribution. The burner was mounted at the top of a 25 cm x 25 cm square-section wind tunnel from where fresh air was flowing at 0.5 m/s to accompany the flow of interest and prevent early mixing with ambient air. The setup allowed measurements from 1 to 20 diameters above the nozzle with no mixing with ambient air, and thus, no intrusion of nitrogen within the probe volume. Consequently, no combustion chamber was required for measurements in the near-field, which was most important for the present investigation of localized extinction in these flames.

The jet flames were axisymmetric, so radial profiles were measured from the central axis to the pure oxidizer region, to ensure capturing the full reaction zone. To obtain the profiles, the 6-mm probe was translated by steps of 3 mm, with a minimum of 500 shots systematically acquired for each step. When crossing the reaction zone, as many as 1500 shots were recorded to improve the quality of the data.

The calibration and data processing method used for laser Raman scattering was the recently developed hybrid method described in [19]. The method is based on the Ramses spectral simulation code [20], which generates Raman spectral libraries for the major species over temperatures ranging from 290 K to 2500 K, for optically well characterized detection setups. Coupled with a short series of calibration measurements (practically one per species), the main calibration coefficients required to process the Raman data can be known by integrating the spectral libraries over regions corresponding to the on-chip binning. However, not everything was solved by the Ramses code. Since the code is based on quantum mechanical models, reliable spectra simulations for methane, for instance, are not available over the whole temperature range of interest. Thus, the remaining calibration coefficients still had to be found through direct measurements over a large temperature range. For example, the temperature dependent calibration curves for CH_4 Raman response and CH_4 crosstalk onto other species were determined

from measurements of an electrically heated CH_4/N_2 mixture between room temperature and about 950 K. Extrapolation to flame temperatures was tested by comparing measurements and Chemkin calculations of laminar partially premixed CH_4/air jets flames and opposed flow flames [11].

CO mass fraction could locally reach up to 0.18 in these oxy-fuel flames, and there is no crosstalk from N_2 onto the CO Raman channel in these flames, which are free of N_2. Consequently, CO-Raman measurements are of better quality in the present flames than in typical CH_4/air flames and are reported here in favour of the CO-LIF measurements. Additionally, measurements of pure cold CO were added to the calibration procedure to improve the accuracy of the calibration. The CO Raman response at higher temperature was calculated from Ramses libraries [19, 20] in reference to the cold calibration. In air-diluted flames, the CO-LIF measurements are used in favour of the CO-Raman measurements, and the CO calibration is done in a fuel-rich, premixed laminar flame in order to minimize uncertainty in the effects of collisional quenching.

Signals were corrected for CCD background, flat field, total Nd:YAG laser energy, interferences from laser induced fluorescence in Raman signals, broadband flame luminosity, beam steering through flames, and bowing effect through Raman optics [19]. Data were filtered for sparks and dusts particles altering Rayleigh and Raman signals, although such events were rare since in-line particle filters had been installed along the critical gas lines.

Table 2. Representative uncertainties of scalar measurements at flame conditions

Scalar	Standard deviation (%)	Accuracy (%)	Premixed flame
T	1.3	2	Φ = 0.97, T = 2185 K
N_2	1.1	2	Φ = 0.97, T = 2185 K
CO_2	4.5	4	Φ = 0.97, T = 2185 K
H_2O	4.1	3	Φ = 0.97, T = 2185 K
Φ	3.1	5	Φ = 0.97, T = 2185 K
CO	6.7	8	Φ = 1.28, T = 2045 K
H_2	9.2	8	Φ = 1.28, T = 2045 K

Table 2 lists the uncertainties calculated from laminar premixed CH_4/air flat flames, based on the standard deviation (precision) and the estimated accuracy of averaged measurements. The standard deviation is mostly higher than in [18], due to the lower laser energy (approximately 1 J/pulse instead of 1.8 J/pulse, limited by the availability of only three of four lasers and the need to avoid optical breakdown in the coflow mixture) and to about 15 % transmission loss through the Schott KG2 glass filter. The estimated accuracy is mostly the same as in [18], except for CO and H_2, whose Raman calibration is based on pure gas measurements at ambient temperature, leading to better accuracy. In non-premixed oxy-fuel flames, accuracy for CO is expected to be better, since CO levels are higher and there is no crosstalk from N_2, though this positive effect may be locally balanced by interferences from laser induced fluorescence (cf. Section 4.5). The accuracy at low temperatures for the reactants from the oxy-fuel flames is also expected to be better, since they are calibrated with pure gas measurements at ambient temperature. However, relative uncertainties in the mean values increase for all reactive species as their mass fractions

decrease. All flows were measured using mass flow controllers which were calibrated (within 1 % of reading) against laminar flow elements. The mixture fraction was calculated from the measured mass fractions using the Bilger formulation [21]. The measurement limits are discussed in Sections 4.5 and 4.6, in the context of the reported results.

4.   Results and Discussion

Most of the following analysis will deal with the progression of the flame structure in the A- and B-series of flames, and will rely on the analysis of Favre-averaged radial profiles of selected mass fractions, measured conditional scalar statistics in mixture fraction space, and results from laminar diffusion flame calculations. First, the focus will be set on the evolution of the localized extinction, followed by an investigation on the influence of differential diffusion. Then, the CO measurements and the shift of the maximum flame temperature from stoichiometry will be commented. Lastly, the measurement limits and the main particularities seen for CO_2-diluted oxy-fuel flames compared to air-diluted flames while using Raman/Rayleigh laser diagnostics will be discussed.

4.1. Localized extinction

Localized extinction occurs when turbulent mixing rates become competitive with critical rates of chemical reactions. The phenomenon induces local temperature drops due to increasing heat removal rates from convection and diffusion along with decreasing chemical reaction rates [22].
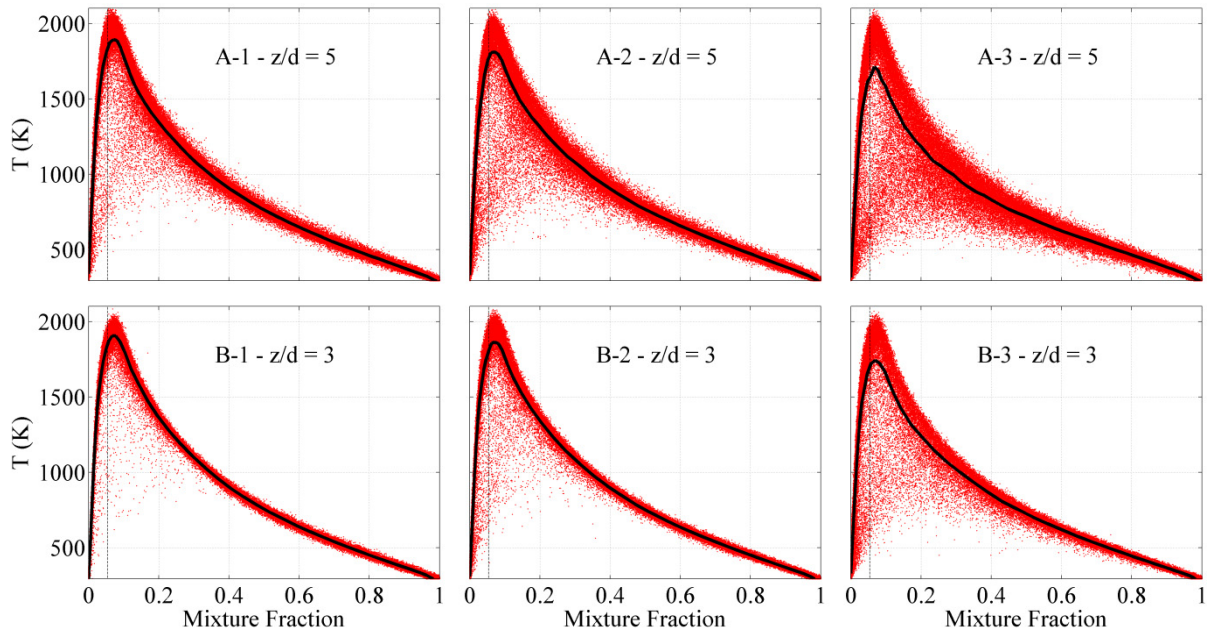
Fig. 1. Scatter plots of Rayleigh temperature at z/d = 5 for A-series and at z/d = 3 for B-series. The conditional mean temperature is plotted with a solid line. The stoichiometric mixture fraction is marked by a vertical dashed line.

Scattered plots of Rayleigh temperature versus mixture fraction for both flame series are shown in Fig. 1. Each dot represents the result of a single-shot measurement from various locations along the radial axis. Dots scattered below the narrow, dense band of temperature indicate localized extinction. Barlow et al. [16] reported that extinction roughly took place around four diameters above the nozzle within the $CH_4/H_2/air$ flames that were studied. Similarly, extinction tended to happen within this area in the present flame series. The probability of localized extinction gradually increased by lowering the H_2 content in fuel as seen with the A-series or by increasing Re_{Fuel} as seen with the B-series. This result was expected, as lowering the H_2 content in fuel decreases the chemical reaction rate, and increasing Re_{Fuel} increases the mean scalar dissipation rate, both rates being essential in the localized extinction mechanism.

Figure 1 shows that the samples deviating from the narrow band of temperature were especially located between 600 and 1700 K and the evolution of probability of localized extinction did not significantly affect the behaviour of the narrow band of temperature, representing fully reacting states or flamelets. The conditional mean of temperature, shown by the black solid lines, decreased only moderately for the observed levels of localized extinction.

Figure 2 shows pictures of the two series of turbulent jet flames, taken using a very low exposure time to help reveal patterns from the flame structure. Flames A-1 and B-1 visually appeared to be fully burning even though they displayed in Fig. 1 a non-negligible number of samples deviating from the narrow band of temperature. During the preliminary phase of defining the flame conditions, H_2 molar fraction of 60 % in fuel was tested and displayed even fewer samples out of the narrow band of temperature (not shown here), as expected since H_2 considerably improves the local stability of flames by increasing the chemical reaction rate.
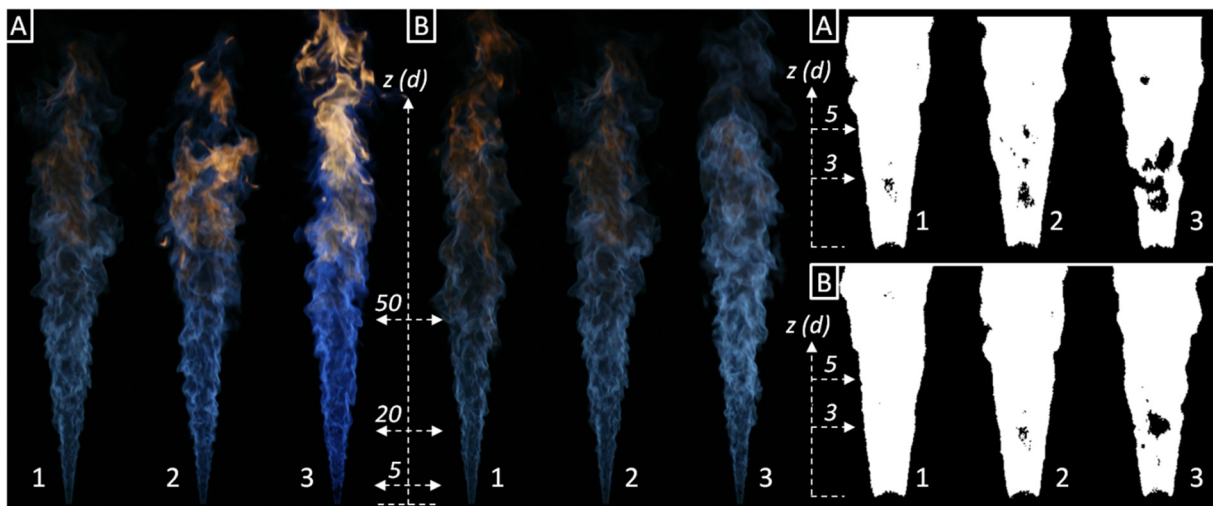

Fig. 2. Pictures of A-series flames (left), B-series flames (centre) and close-ups from the region of localized extinction for A-series (top-right) and B-series (bottom-right). Close-ups were post-processed by applying a threshold to highlight the localized extinction. Exposure time: 1/2500 s, ISO: 1600.

A chosen sample of flame pictures was binarized with a fixed threshold and allowed enhanced visualization of the localized extinction as areas of reduced visible luminosity (see Fig. 2, right). The shape and exact location were constantly changing, though the phenomenon tended to

systematically appear between 3 and 5 diameters above the nozzle. Localized extinction events appeared very intense on Flame A-3, as shown in Fig. 2 (top-right). Note that, for a given flame, effects from localized extinction do not necessarily appear on every picture as clear as in the chosen sample, notably due to the line of sight visualization, though the chosen sample is quite representative.

By lowering the H_2 molar fraction in fuel below 37 %, localized extinction systematically became more frequent, leading to lift-off or flame blow-off. Similarly, increasing further Re_{Fuel} up to around 20,000 also lead to lift-off and instabilities. These conditions were certainly the threshold of the unbalanced competition between heat removal rate and chemical reaction rate.

Results from Raman/Rayleigh diagnostics brought systematic and reliable information. The conditional means of mass fraction for CO, H_2, O_2 and H_2O are plotted with the mixture fraction in Fig. 3 for both flame series, at three different axial positions, intercepting the region of localized extinction. Similarly, the Favre-averaged mass fractions of CO, H_2, O_2 and H_2O are plotted with the radial position in Fig. 4. Note that, measurements performed at 1 diameter above the nozzle revealed mass fraction profiles very similar for each series and thus, are not shown here. By looking at O_2 mass fraction at 3 or 5 diameters above the fuel nozzle in Fig. 3 and 4, it can be seen on the fuel-rich side that unburnt oxidizer penetrated into the fuel-rich part of the jet, with lower H_2 content in fuel or higher Re_{Fuel}. This was a direct consequence of localized extinction, which seemed to vanish out farther downstream.

In Fig. 3 and 4, the levels of H_2O and CO gradually decreased around the localized extinction zone, respectively with decreasing the H_2 content in fuel in the A-series, and with increasing the jet Reynolds number in the B-series. This variation was mostly induced by the increase of O_2 mass fraction in the reaction zone. However, this was slightly more intense in the A-series and could be explained by the variation of fuel composition, coupled with lower jet exit speeds. Farther downstream, far from the localized extinction, the decreased levels in H_2O and CO were still visible for the A-series. A slight increase in CO_2 mass fraction was also found but is not shown here. For the B-series, fuel and oxidizer compositions are the same for each flame, only the jet and coflow speeds were varied.

In Fig. 3 and 4, the root-mean square (RMS) fluctuations of CO mass fractions for Flame A-1 and B-1 are shown by grey areas. They enable to see the significant amplitude of the local fluctuations, which are mainly due to turbulent intensity. However, for Flame A-1, effects of localized extinction may have contributed to the amplitude of the RMS fluctuations, which appears larger than for Flame B-1.
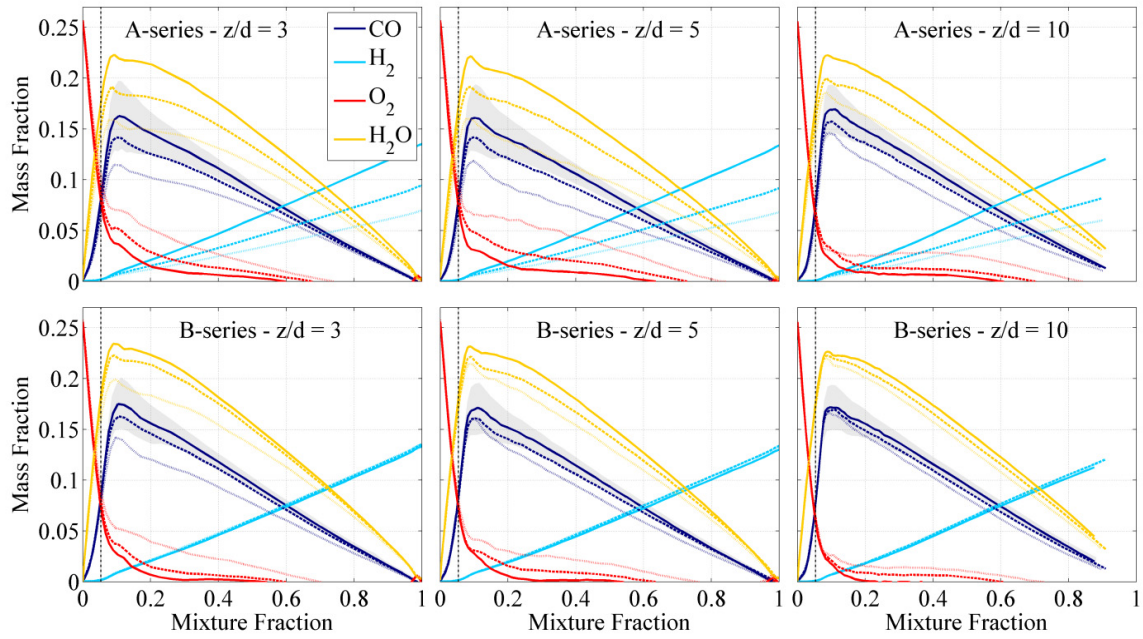
Fig. 3. Conditional means for CO, H_2, O_2 and H_2O mass fractions for both A- and B-series at z/d = 3, 5 and 10. Flames A-1 and B-1 are shown with solid lines, A-2 and B-2 with dashed lines, and A-3 and B-3 with dotted lines. The stoichiometric mixture fraction is marked by a dashed line. The grey area represents the conditional RMS fluctuations for CO mass fraction corresponding to Flames A-1 and B-1.
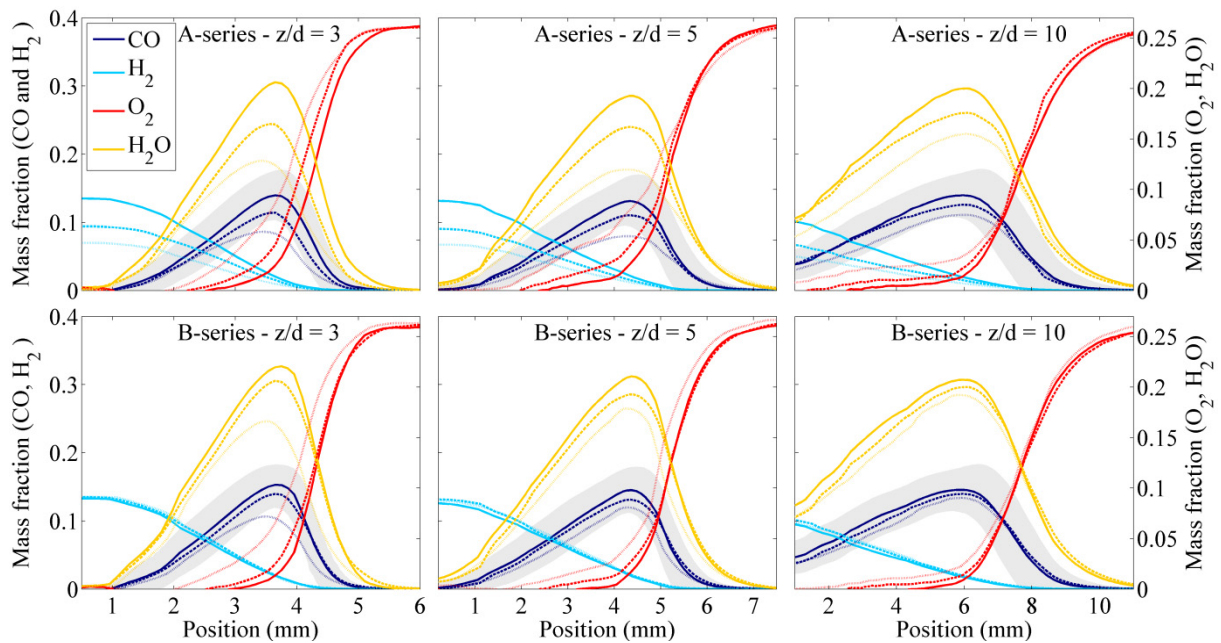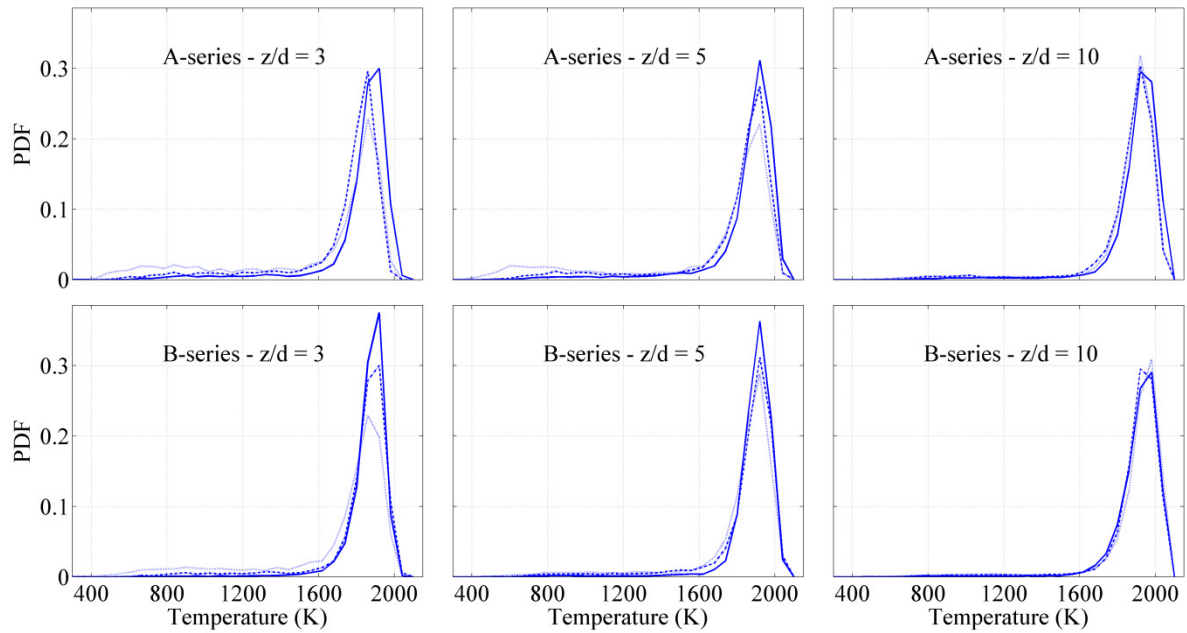

Fig. 4. Favre-averaged radial profiles for CO, H_2, O_2 and H_2O mass fractions for both A- and B-series at z/d = 3, 5 and 10. Flames A-1 and B-1 are shown with solid lines, A-2 and B-2 with dashed lines, and A-3 and B-3 with dotted lines. The grey area represents the RMS fluctuations (according to the Favre decomposition) for CO mass fraction corresponding to Flames A-1 and B-1.

Fig. 5. PDF of the temperature within a narrow band in mixture fraction (total width 2 Δ = 0.04) centred on the locus of maximum temperature for both A- and B-series at z/d = 3, 5 and 10. Flames A-1 and B-1 are shown with solid lines, A-2 and B-2 with dashed lines, and A-3 and B-3 with dotted lines.

Figure 5 shows the probability density function (PDF) of the temperature for both flame series at 3, 5 and 10 diameters above the nozzle. The PDF of the temperature is calculated for each profile only on a narrow band, 2Δ, of mixture fraction centred on the locus of maximum temperature. In the present study, Δ is chosen equal to 0.02 to include a representative number of temperature measurements in the PDF calculation. The number of temperature measurements used for the PDF is about the same for each flame at a given axial location, from about 6000 measurements at z/d = 3 to about 13,000 at z/d = 10. Within each plot, only one parameter is varied: hydrogen content in the fuel for the A-series and jet Reynolds number in the B-series. In addition, the adiabatic flame temperature is similar from one flame to another. Thus, any variation of the PDF of the temperature for a given axial location can be mostly attributed to a variation of the degree of localized extinction inducing local temperature drops. At 10 diameters above the nozzle, above the region of localized extinction, all flames display very similar profiles of PDF of the temperature. At 3 and 5 diameters above the nozzle, lower and higher temperatures can be clearly distinguished into two zones. Higher temperatures correspond to the fully burning mixtures and systematically display a peak. For the A-series, the PDF of the temperature within this range decreases with the H_2 content in the fuel. For the B-series, the same trend can be observed while increasing the jet Reynolds number, though it is clearer at 5 diameters above the nozzle than at 3 diameters. The decreased contribution from the higher temperatures is balanced by an increased contribution from the lower temperatures, and especially from the very low temperatures, suggesting an increased content in fresh gases. These observations can be correlated to the corresponding higher presence of oxygen and lower presence of flame products in the flame region, as seen in Fig. 3 and 4.

One further way to quantify the degree of localized extinction is to define a fully burning probability (*FBP*), based on the same definition of the PDF of the temperature above. FBP is calculated as the PDF within a 2Δ narrow band of mixture fraction centred on locus of maximum temperature, corresponding to the temperatures above a threshold temperature, T_{lim}, and plotted with the measured axial locations (see Fig. 6). T_{lim} should be reasonable, well below the calculated adiabatic temperatures (~2250 K for all the present flames) and still relatively high. As seen in Fig. 5, T_{lim} = 1700 K appears as a good trade-off to capture localized extinction effects on temperature within the present flames.
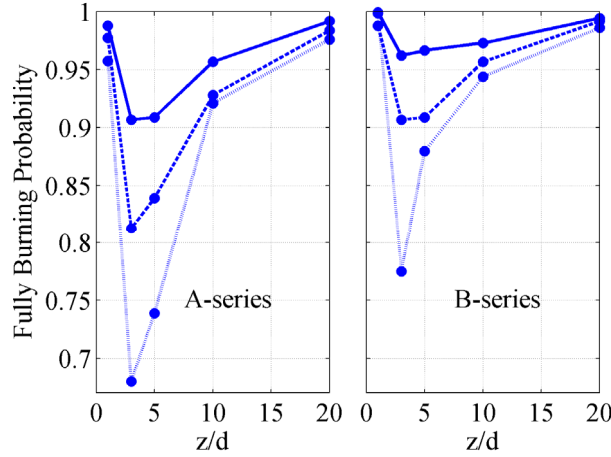

Fig. 6. Fully burning probability plotted with axial location for both flame series, based on the PDF of the temperatures above T_{lim} = 1700 K, within a narrow band in mixture fraction (total width 2Δ = 0.04) centred on the locus of maximum temperature. A-1 and B-1 are shown with solid lines, A-2 and B-2 with dashed lines, and A-3 and B-3 with dotted lines.

FBP is equal to 1 when all measured temperatures from the sample are above T_{Lim}, thus the sample is considered as in a fully burning state. On the other hand, *FBP* is equal to 0 when those temperatures are all below T_{Lim}, meaning that locally, the flame is supposedly close to blow-off. A flame showing an axial profile with constant *FBP* equal to 1 would be considered as fully burning over its whole measured length.

It can be seen in Fig. 6 that, according to the *FPB* criterion, none of the present flames was fully burning, though Flame B-1 was reasonably close. Fig. 6 also shows that localized extinction happened systematically between 1 and 5 diameters above the nozzle and its effect vanished out downstream since all profiles seemed to tend to *FBP* = 1. As expected, Flame A-3 appeared to have the most dramatic *FBP* of the two series. At 1 diameter above the nozzle, the *FBP* criterion gradually decreased for the A-series as the molar fraction of H_2 in the fuel decreased, showing a more dramatic effect on the very near field than for the B-series. Only a few axial locations have been measured and a finer resolution would be required to draw further conclusions.

Another way to quantify the degree of extinction is to calculate the burning index based on temperature (*BI_T*). Details and limits about it can be found in the literature [16, 23-25]. BI_T is generally calculated as the ratio of the difference between local instantaneous temperature and room temperature, and the difference between reference temperature and room temperature.

For hydrocarbon flames, the reference temperature represents a fully burnt state at a given mixture fraction, and is typically taken a laminar flame calculations at low strain rate from an arbitrary chosen flame composition. BI_T is then usually plotted with the mixture fraction.

FBP has been used in the present study in favour of BI_T since it enables to integrate the whole set of temperature measurements into one comprehensive plot against the streamwise location. It enables to spatially bound the localized extinction zone and to compare its streamwise influence on flames from series of similar composition. However, FBP has the disadvantage of being sensitive to two arbitrary-defined parameters and requires a certain number of measurements in the streamwise direction to be properly resolved.

4.2. Influence of differential diffusion

In turbulent non-premixed flame calculations, to greatly simplify the mixing problem, it is often assumed that energy diffuses at the same rate for all species, i.e. the diffusivities are set equal for all species [22], giving the so-called equal diffusivities transport model. However, in the near field of simple jet flames at low to moderate Reynolds number, this assumption is known to be inaccurate as diffusion effects tend to strongly influence the mixing process. The phenomenon has been especially seen at low Reynolds numbers and with high H_2 content in the fuel [11-13]. Thus, changes in the relative importance of molecular diffusion and turbulent transport were expected in the near-field of the present flames.

To evaluate the influence of differential diffusion, laminar diffusion flame calculations were performed with CHEMKIN-PRO [26] using the opposed-jet reactor with the GRI 3.0 mechanisms [27]. Considering non-premixed flames as an ensemble of laminar non-premixed flamelets, results from those calculations could be locally comparable to the experimental results. The purpose was not to simulate the investigated flames but simply to bring into the light underlying physics from the results by isolating some cases locally close to flamelet calculations. Results were compared to the present flames using similar fuel and oxidizer compositions and the two different transport models: full multi-component transport and equal diffusivities. The full multi-component transport model takes into account the effect of differential diffusion, whereas the equal diffusivities assumption sets all species diffusivities equal to the thermal diffusivity (Lewis number equal to 1). Note that radiation effects were included in the calculations and the strain rate was defined as in [28].

In turbulent non-premixed jet flames, one could expect to match a location in the near-field with a relatively high strain rate, whereas a location farther downstream would rather match with a lower strain rate [29]. Focusing especially on Flame B-1, more relevant in this case since closer to a fully burning state (see Fig. 6), and on CO mass fraction, a good match was found with a strain rate $a = 800$ s^{-1} at $z/d = 1$ and $a = 15$ s^{-1} at $z/d = 20$, with full multi-component transport model, as shown in Fig. 7.

In turbulent non-premixed jet flames, the shear layer develops downstream by forming larger-scale turbulent structures until stirring the whole reaction zone, so that those structures control the local mixing rates. Thus, the effects of differential diffusion are expected to be more significant closer to the nozzle, as reported from different flames burning hydrogen [30, 31]; whereas equal

diffusivities transport model would rather match far downstream zones where the upstream effects of differential diffusion have been washed out through a process of re-entrainment and turbulent mixing over the development length of the jet [29].

Figure 7 shows the scatter plots of CO, O_2, H_2, H_2O, CO_2 and CH_4 mass fractions compared to the laminar flame calculations. At 1 diameter above the nozzle, most results agree well with the full multi-component transport model, even though CH_4 and H_2 mass fractions seem to rather agree with the equal diffusivities assumption. At 20 diameters above the nozzle, the results are settled between the two different models. However, after only a few diameters above the nozzle, products start to be present on both sides of the flame region, leading to unclear conclusions for the relative importance of differential diffusion in the mixing process.

One way to quantify the degree of differential diffusion is to calculate the differential diffusion parameter, Z, defined as the difference between the elemental mixture fractions of hydrogen atoms (F_H) and carbon atoms (F_C); see details in [29]. Fig. 8-9 show the results for A- and B-series of flames at 1, 3 and 20 diameters above the nozzle compared to the laminar flame calculations corresponding to similar fuel and oxidizer compositions. RMS fluctuations for A-1 and B-1 are also shown.
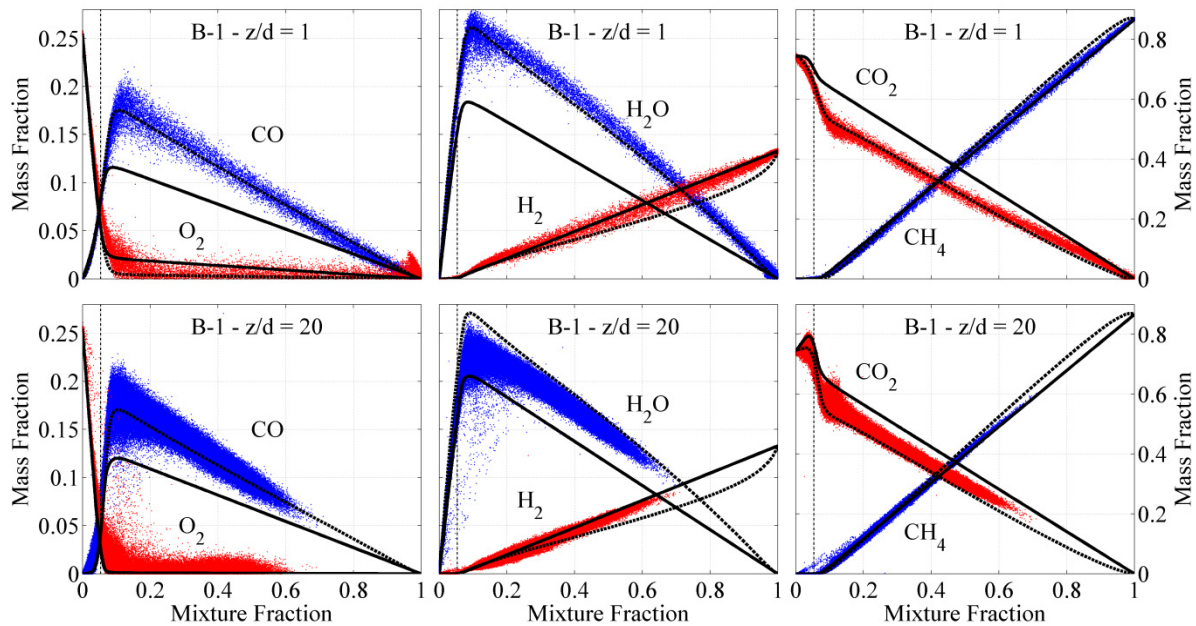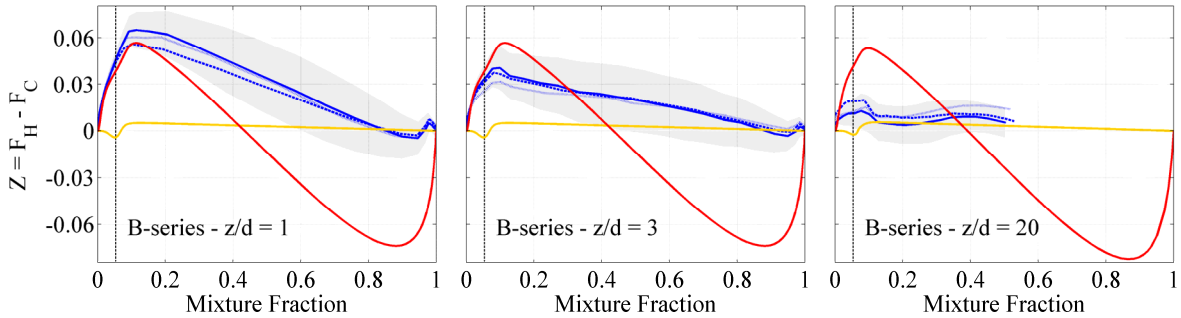

Fig. 7. Scatter plots of mass fractions plotted versus the Bilger mixture fraction for Flame B-1 at z/d = 1 and 20. Corresponding results from laminar flame calculations for strain rates of 800 s^{-1} (top) and 15 s^{-1} (bottom) are plotted using the two different transport models: full multi-component transport (dashed lines) and equal diffusivities (solid lines). The stoichiometric mixture fraction is marked by a vertical dashed line.

Figures 8 and 9 show that the maximum of differential diffusion parameter close to stoichiometric mixture fraction considerably decreased with the axial location, showing good agreement with the expectations. A second observation, especially seen at *z/d* = 1, is that the differential diffusion parameter agrees well with the full multi-component transport model on the lean side of the reaction zone and then shows a major departure from this model toward the

equal diffusivities transport model on the rich side. Indeed, close to the nozzle, the reaction zone and lean side of the flame were in a laminarized part of the flow, so that there, the mixing was mostly controlled by molecular diffusion. However, the rich inner part of the mixing layer was still relatively cold and strongly affected by the pipe flow turbulence. This is likely to explain the behaviour of H_2 and CH_4 mass fractions in Fig. 7 and the major departure from the full multi-component transport model toward the equal diffusivities transport model in the rich side of the flame in Fig. 8-9.
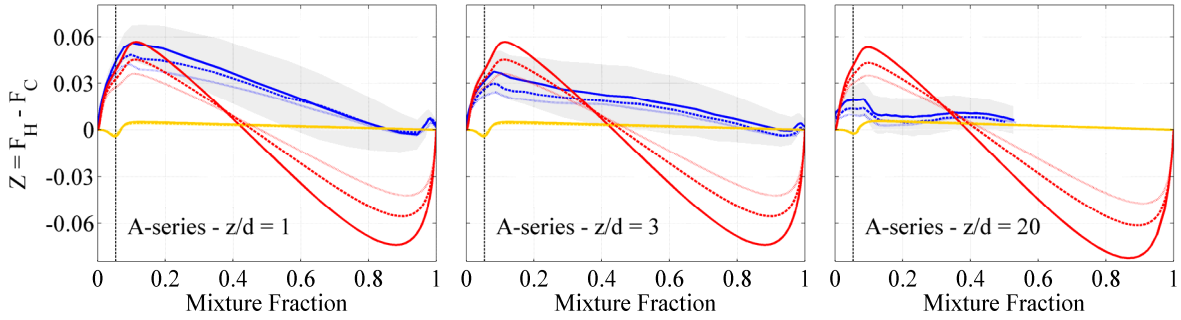
Fig. 8. Differential diffusion parameter Z plotted with the Bilger mixture fraction for A-series flames at z/d = 1, 3 and 20. A-1 is shown with blue solid lines, A-2 with blue dashed lines, and A-3 with blue dotted lines. Corresponding results from laminar flame calculations using A-1 (solid lines), A-2 (dashed lines) and A-3 (dotted lines) fuel and oxidizer compositions with strain rates of 800 s^{-1} (left and centre) and 15 s^{-1} (right) are plotted using the two different transport models: full multi-component transport (red lines) and equal diffusivities (orange lines). The grey area represents the conditional RMS fluctuations for Z corresponding to Flame A-1. The stoichiometric mixture fraction is marked by a vertical dashed line.

Fig. 9. Differential diffusion parameter Z plotted versus the Bilger mixture fraction for B-series flames at z/d = 1, 3 and 20. B-1 is shown with blue solid lines, B-2 with blue dashed lines, and B-3 with blue dotted lines. Corresponding results from laminar flame calculations using B-series fuel and oxidizer compositions with strain rates of 800 s^{-1} (left and centre) and 15 s^{-1} (right) are plotted using the two different transport models: full multi-component transport (red solid line) and equal diffusivities (orange solid lines). The grey area represents the conditional RMS fluctuations for Z corresponding to Flame B-1. The stoichiometric mixture fraction is marked by a vertical dashed line.

The differential diffusion parameter was determined by subtracting two uncertain values. In Fig. 8 and 9, the difference between the measurements was not significant compared to the

corresponding RMS fluctuations. Despite the high level of uncertainty of Z, Fig. 8 seems to show a dependence of the differential diffusion with the CH_4/H_2 ratio. This is confirmed with the laminar flame calculations using A-1, A-2 and A-3 fuel and oxidizer compositions showing that the maximum of the differential diffusion parameter seems to decrease while decreasing the hydrogen molar fraction in the fuel. This result underlines the relative importance of differential diffusion effects in flames where H_2 is mixed with a heavier gas in the fuel stream. Nevertheless, no clear conclusions can be made about the jet Reynolds number dependence of the differential diffusion effects in the B-series flames in Fig. 9.

4.3. High CO levels

The conditional mean CO mass fraction could locally reach up to 0.18 (see Fig. 3, Flame B-1 and z/d = 3). Such high CO mass fractions result from high CO_2-dilution levels. Previous investigations with CO_2-dilution [32, 33] have concluded that CO_2 was not inert but competed primarily with O_2 for atomic hydrogen and lead to formation of CO through the reaction *CO_2 + H <-> CO + OH*. CO concentration is then expected to be locally higher than with air-dilution. Another conclusion was that the rate of the reaction converting CO_2 into CO would decrease as the turbulent mixing rates increase up to reaching the forward rate of this reaction. The conditional mean of CO mass fraction showed in Fig. 3 for the B-series seems to agree with this trend, though it remains unclear because of the effects of localized extinction.

Heil et al. [34], who performed measurements in CO_2-diluted oxy-fuel flames in a furnace for flameless combustion, showed that high CO levels in the products are very sensitive to the O_2/CO_2 ratio. In low dilution oxy-fuel flames, high flame temperature would also contribute to increased local CO concentration through CO_2 dissociation. CO levels up to 30 % were found in pure oxygen flames [4]. In the present study, the O_2/CO_2 ratio was kept constant. Further investigation with a varying O_2/CO_2 ratio would be of great interest.

4.4. Shift of maximum temperature from stoichiometry

Figure 10 shows the scatter plots of temperature in mixture fraction space and the corresponding results from laminar flame calculations using the two transport models. A close-up was made on the flame region. Close to the nozzle, the temperature peak shows best agreement with the laminar flame calculation using full multi-component transport model, which tends to be slightly shifted toward the rich side compared to results with equal diffusivities transport model. This observation is verified for both Flame B-1 and Flame A-3, in spite of their significantly different CH_4/H_2 ratio. From z/d = 1 to z/d = 5, the temperature peak is greatly shifted back toward the lean side. Then, it seems to remain at a constant location in mixture fraction space until z/d = 20. The laminar flame calculations also show a similar trend when reducing considerably the strain rate from 800 s^{-1} to 15 s^{-1}. However, the shift for the laminar flame calculations using full multi-component transport model appears to be more dramatic than with the equal diffusivities transport model.

This trend can be explained by the relative importance of differential diffusion when the reaction zone is still very thin in the near field, which probably enhances the diffusion of small molecules such as H_2 through the reaction zone. As the reaction zone thickens farther

downstream, the relative importance of differential diffusion decreases. This phenomenon is seen in Fig. 10 over the development length of the jet until a region between z/d = 5 and z/d = 10, where differential diffusion does not seem to interact any more with the location of the temperature peak.

Law et al. [35] investigated the cause for the shifting of the maximum adiabatic flame temperature from stoichiometry. The authors concluded that the phenomenon is a consequence of reduced heat release in the presence of product dissociation. Thus, in the present case, there would be more dissociation in the lean side, so that the heat release peaks on the rich side, inducing the rich shift of the maximum flame temperature. The shift may be more pronounced than with air-dilution, due to the high CO_2 content on the lean side, characterized by higher heat capacity and lower heat release than N_2.
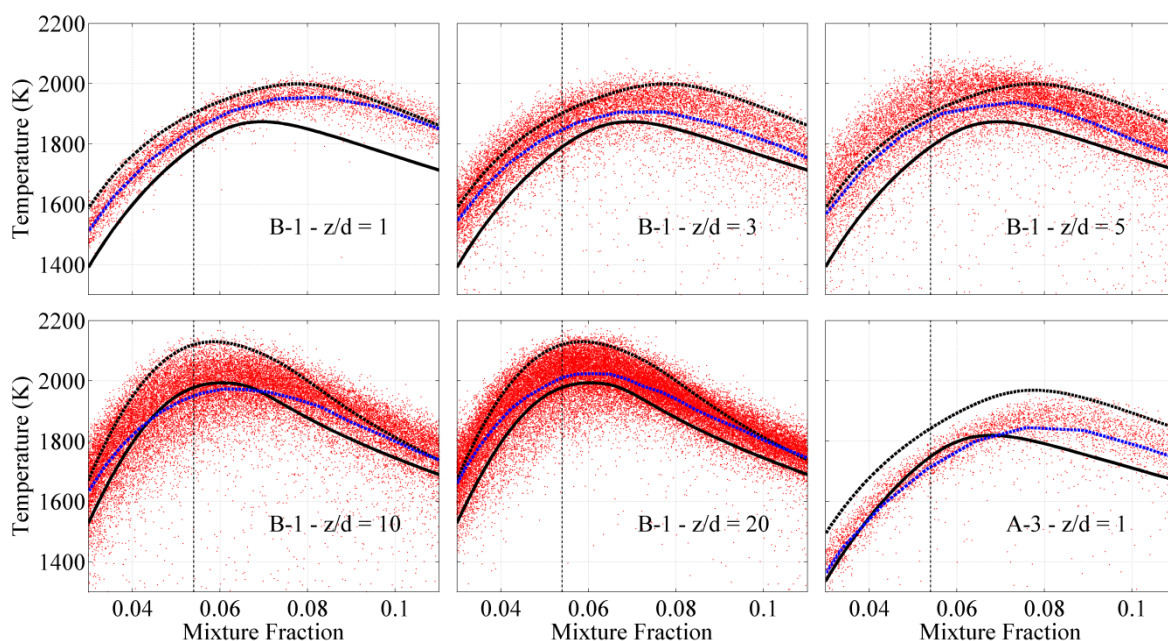

Fig. 10. Scatter plots of Rayleigh temperature with mixture fraction for Flame B-1 at z/d = 1, 3, 5, 10 and 20 and for Flame A-3 at z/d = 1. The conditional mean is plotted with a blue dashed line. Results from laminar flame calculations corresponding to fuel and oxidizer composition of displayed flame are plotted for strain rates of 800 s^{-1} (top row and bottom-right), and 15 s^{-1} (bottom-left and -centre). The two transport models were used in the calculations: full multi-component transport (dashed lines) and equal diffusivities (solid lines). The multi-component solution lies above the equal diffusivities solution in both cases. The stoichiometric mixture fraction is marked by a vertical dashed line.

Figure 11 gives another view of the results from the laminar diffusion flame calculations. Mixture fractions corresponding to the peak of adiabatic temperatures, T_{Ad-Max} have been plotted within a range of strain rates from 10 to 1000 s^{-1}. Results show that, at very low strain rates, T_{Ad-Max} peaks rather close to the stoichiometric mixture fraction for both transport models. However, at higher strain rates, the temperature peak tends to be shifted toward the rich region of the mixture fraction space. For strain rates from 500 to 1000 s^{-1}, this trend seems to get slightly attenuated with the equal diffusivities transport model but keeps on with the full multi-

component transport model, for which the shift of $T_{Ad\text{-}Max}$ peak toward the rich region is more dramatic. In fact, the flame thickness is decreased as the strain rate is increased, which consequently acts on the residence time. Thus, at low strain rates, the mixing time is longer than the reaction time, so that the system is close to follow the ideal assumption of fast chemistry. In this case, $T_{Ad\text{-}Max}$ would peak at stoichiometric mixture fraction and the transport phenomena would not affect much the temperature peak shift. On the other hand, at higher strain rates, the mixing time becomes shorter than the reaction time, potentially leading to incomplete reactions and stronger effects of the transport phenomena.
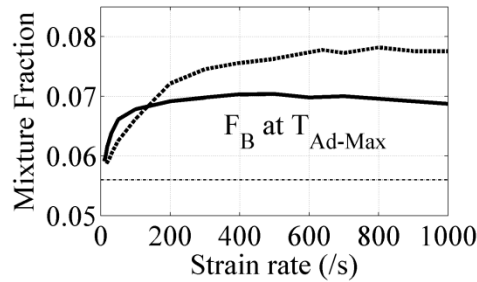

Fig. 11. Mixture fraction at maximum adiabatic flame temperature from laminar diffusion flame calculations corresponding to fuel and oxidizer composition of flames A-1, B-1, B-2 and B-3. Results are plotted with the strain rate. The two transport models were used in the calculations: full multi-component transport (dashed lines) and equal diffusivities (solid lines). The stoichiometric mixture fraction is shown by a horizontal dashed line.

4.5. Discussion of measurement challenges

During the measurements, flames displayed trends concerning soot formation at the flame tip (see Fig. 2). By reducing the H_2 content in fuel, A-series flames produced visible soot farther upstream, in part due to lower speeds at the jet exit for the same jet exit Reynolds number (see Table 1), the correspondingly longer residence time for soot formation, and the higher hydrocarbon species concentration. A similar trend was revealed with B-series flames while lowering Re_{Fuel}. As seen in Fig. 2, soot formation actually reached easily visible levels in Flame A-3.

The magnitude and spectroscopic distributions of hydrocarbon fluorescence interferences on the Raman measurements vary in these flames, depending on fuel composition, Reynolds number, and spatial location. Generally, measured interference levels increased with downstream distance in each flame, due to increasing residence time. At a given downstream location, hydrocarbon fluorescence interference decreased with increasing H_2 fuel fraction and with increasing Reynolds number.

Corrections for these hydrocarbon fluorescence interferences are not perfect and leave some residual errors, particularly in regions of high interference on the fuel-rich side of the reaction zone. These residual errors can be seen, for example, in O_2 and CO mass fraction results (see Fig. 3), which can be over- or under corrected by around 1 %, often appearing as a wrinkle in the plots. Similarly, an unrealistic wrinkle tended to appear for O_2 mass fraction in Fig. 3-4 and 7 and

for Z in Fig. 8-9, corresponding to mixture fractions close to 1. These imperfections are most likely due to the Raman cross-talk of CH_4 onto O_2, which is sensitive to very slight fluctuations where CH_4 is present in large quantities. This consequently affected other species mass fraction.

Localized extinction phenomena are extremely sensitive to the coflow temperature. A slight temperature variation can have a dramatic effect on flame structure close to blow-off conditions. While with air-diluted combustion, it is generally not a problem to supply large quantity of air at a stable temperature, supplying large quantities of CO_2 was challenging. CO_2 has a much larger Joule-Thomson coefficient than other supplied species, leading to a strong temperature dependence on upstream pressure conditions. An aluminium evaporator had to be coupled to liquid CO_2 tanks, followed by in-line gas heaters and a few dozens of meters of gas pipes, to keep the CO_2 temperature constant at 294 K at the coflow outlet.

More detailed investigation on differential diffusion could be of importance in both flame series since Re_{Fuel} remained close to transition of molecular transport models. An investigation at much higher Re_{Fuel} would have been even more beneficial, but remained physically unfeasible at laboratory scale due to the consequent supply of O_2 and CO_2.

4.6. Discussion of Raman/Rayleigh diagnostics in CO_2-diluted oxy-fuel flames

As for performing laser diagnostics, CO_2-diluted oxy-fuel flames remained very challenging due to their high CO_2 content. For instance, CO_2 has a higher refractive index than air, and this caused some steering of the laser beam when it passed through the unsteady interface between air and the CO_2/O_2 coflow. Another drawback is its high emissivity which creates a significant thermal load. Those two examples had to be taken into account while performing the experiments. Beam steering was not severe using the 32 % O_2 mixture, and the main effects of beam steering are accounted for automatically by the hybrid Raman/Rayleigh processing method [19].

Furthermore, the two Raman bands for CO_2 can reach high intensities relatively to the other species, due to their high Raman cross-section and the Raman scattering linearity with the concentration. Since the Raman spectrum of CO_2 overlaps the detection region of O_2, the induced crosstalk of CO_2 onto O_2 can lead to significant relative uncertainties in the measurement of O_2 if not correctly accounted for in the data processing, especially when the actual concentration of O_2 is low. Raman rotational bands of H_2, mostly neighbouring the CO_2 Raman bands, may also affect the latter when H_2 is present at large quantities, or at high temperatures. Both crosstalk effects are reasonably well handled by the hybrid method.

An important advantage compared to air-diluted conditions is the absence of N_2 in the Raman spectra, which limits the number of Raman species to be processed to six. Besides, N_2 is very close to CO on the Raman spectra. N_2 induces a strong cross-talk onto CO, enhanced by the relatively high concentration of N_2 in air-diluted flames. As previously detailed, detection and quantification of CO could be confidently achieved by laser Raman scattering in favour of laser induced fluorescence techniques.

Varying the oxygen molar fraction in the oxidizer can lead to very high temperatures, for which the radical pool may represent a non-negligible concentration and cannot be ignored any more in the Raman/Rayleigh resolution. In the present flames, a molar fraction of 32 % oxygen in the oxidizer limited the radical pool to a negligible concentration compared to the uncertainties of the diagnostics.

5.   Concluding remarks

Measurements of the temperature and mass fractions of main species were performed in turbulent non-premixed CO_2-diluted oxy-fuel jet flames, using the simultaneous line imaging of Raman/Rayleigh scattering. Two series of three flames burning mixtures of hydrogen and methane in a coflow burner were studied. The objective was to investigate the influence of CH_4/H_2 ratio and jet Reynolds number on localized extinction and flame structure in CO_2-diluted oxy-fuel jet flames.

Consequences of localized extinction in the flame composition could be captured, notably by the scatter plots of temperature in mixture fraction space, at different axial locations. Additionally, higher contents of oxygen on the rich side of the flame front could be observed in the conditional mean of O_2 mass fraction as one progress toward higher probability of localized extinction. Based on the PDF of the temperature, a fully burning probability index able to quantify the degree of extinction along the streamwise location was calculated.

Comparison of conditional mean mass fractions and laminar flame calculations using similar fuel and oxidizer compositions underlined the significant level of differential diffusion in the near-field, due to the very low levels of turbulence in the reaction zone so close to the nozzle. The relative importance of differential diffusion tended to decrease farther downstream as the large-scale turbulent structures tended to develop and control the local mixing rates by stirring the reaction zone.

Due to the high CO_2 content in the oxidizer, CO mass fraction was found to be effectively higher than in comparable air-diluted flames, especially in the near-field. This effect would be due to CO_2 competing primarily with O_2 for atomic hydrogen and leading to formation of CO through the reaction $CO_2 + H \leftrightarrow CO + OH$.

A shift of maximum flame temperature toward the rich side of the mixture fraction space was observed in the measurements. The shift appeared to be greater in the near-field and tended to diminish until z/d = 5, from where the peak location seemed to remain constant. The phenomenon can be a consequence of reduced heat release in the presence of product dissociation, so that more dissociation in the lean side induces the heat release peak on the rich side and a rich shift of the maximum flame temperature.

Results on the whole displayed reasonable accuracy, from 1 up to 20 nozzle diameters above the nozzle. Though levels of hydrocarbon fluorescence were fairly high in some cases, the sensitivity of the detection system also allowed capturing precise hydrogen mass fractions which would make this data relatively interesting for validation of turbulent combustion models. Only

a limited part of the results is shown in the present paper but most data, including scalar fluctuations and conditional statistics, are available upon request.

Acknowledgements

References

[1]   O. Bolland, S. Saether, Energ. Convers. Manage. 33 (5-8) (1992) 467-475.

[2]   O. Bolland, P. Mathieu, Energ. Convers. Manage. 39 (16-18) (1998) 1653-1663.

[3]   Y. Tan, M. A. Douglas, K. V. Thambimuthu, Fuel 81 (8) (2002) 1007-1016 Pii S0016-2361(02)00014-5.

[4]   M. Ditaranto, J. C. Sautet, J. M. Samaniego, Exp. Fluids 30 (3) (2001) 253-261.

[5]   J. C. Sautet, M. Ditaranto, J. M. Samaniego, O. Charon, Int. Commun. Heat Mass 26 (5) (1999) 647-656.

[6]   J. C. Sautet, L. Salentey, M. Ditaranto, Int. Commun. Heat Mass 28 (2) (2001) 277-287.

[7]   E. Croiset, K. V. Thambimuthu, Fuel 80 (14) (2001) 2117-2121.

[8]   M. Ditaranto, J. Hals, Combust. Flame 146 (3) (2006) 493-512 DOI 10.1016/j.combustflame.2006.04.015.

[9]   F. H. V. Coppens, A. A. Konnov, Fuel 87 (13-14) (2008) 2866-2870 DOI 10.1016/j.fuel.2008.04.009.

[10]   P. Kutne, B. K. Kapadia, W. Meier, M. Aigner, Proc. Combust. Inst. 33 (2) (2011) 3383-3390.

[11]   R. S. Barlow, J. H. Frank, A. N. Karpetis, J. Y. Chen, Combust. Flame 143 (4) (2005) 433-449 DOI 10.1016/j.combustflame.2005.08.017.

[12]   M. C. Drake, R. W. Bilger, S. H. Stårner, Proc. Combust. Inst. 19 (1982) 459-467.

[13]   L. L. Smith, R. W. Dibble, L. Talbot, R. S. Barlow, C. D. Carter, Combust. Flame 100 (1-2) (1995) 153-160.

[14]   L. Wang, N. E. Endrud, S. R. Turns, M. D. D'Agostini, A. G. Slavejkov, Combust. Sci. Technol. 174 (8) (2002) 45-72 10.1080/00102200290021245.

[15]   M. Ditaranto, T. Oppelt, Exp. Therm. Fluid Sci. 35 (7) (2011) 1343-1350.

[16]   R. S. Barlow, H. C. Ozarovsky, A. N. Karpetis, R. P. Lindstedt, Combust. Flame 156 (11) (2009) 2117-2128 DOI 10.1016/j.combustflame.2009.04.005.

[17] D. C. Haworth, Prog. Energ. Combust. Sci. 36 (2) (2010) 168-259 DOI 10.1016/j.pecs.2009.09.003.

[18] R. S. Barlow, G. H. Wang, P. Anselmo, M. S. Sweeney, S. Hochgreb, Proc. Combust. Inst. 32 (2009) 945-953 DOI 10.1016/j.proci.2008.06.070.

[19] F. Fuest, R. S. Barlow, D. Geyer, F. Seffrin, A. Dreizler, Proc. Combust. Inst. 33 (1) (2011) 815-822.

[20] D. Geyer, 1D-Raman/Rayleigh Experiments in a Turbulent Opposed-Jet, PhD Thesis, TU Darmstadt, VDI-Verlag, Düsseldorf (2005) ISBN 3-18-353306-5.

[21] R. W. Bilger, S. H. Starner, R. J. Kee, Combust. Flame 80 (2) (1990) 135-149.

[22] J. Warnatz, U. Maas, R. W. Dibble, Combustion, Springer 3rd Edition (2000).

[23] R. R. Cao, S. B. Pope, Combust. Flame 143 (4) (2005) 450-470 10.1016/j.combustflame.2005.08.018.

[24] A. R. Masri, P. A. M. Kalt, Y. M. Al-Abdeli, R. S. Barlow, Combust. Theor. Model. 11:5 (2007) 653-673.

[25] J. Xu, S. B. Pope, Combust. Flame 123 (3) (2000) 281-307.

[26] CHEMKIN-PRO, Reaction Design: San Diego, 2008.

[27] G. P. Smith, D. M. Golden, M. Frenklach, N. W. Moriarty, B. Eiteneer, M. Goldenberg, C. T. Bowman, R. K. Hanson, S. Song, W. C. Gardiner, V. V. Lissianski, Z. Qin, http://www.me.berkeley.edu/gri_mech/.

[28] Z. Cheng, J. A. Wehrmeyer, R. W. Pitz, Combust. Sci. Technol. 178 (12) (2006) 2145-2163 Doi 10.1080/00102200600616745.

[29] R. S. Barlow, G. J. Fiechtner, C. D. Carter, J. Y. Chen, Combust. Flame 120 (4) (2000) 549-569.

[30] W. Meier, A. O. Vyrodov, V. Bergmann, W. Stricker, Appl. Phys. B-Lasers O. 63 (1) (1996) 79-90.

[31] V. Bergmann, W. Meier, D. Wolff, W. Stricker, Appl. Phys. B-Lasers O. 66 (4) (1998) 489-502.

[32] A. R. Masri, R. W. Dibble, R. S. Barlow, Combust. Flame 91 (3-4) (1992) 285-309.

[33] P. Glarborg, L. L. B. Bentzen, Energ. Fuels 22 (1) (2008) 291-296 Doi 10.1021/Ef7005854.

[34] P. Heil, D. Toporov, M. Forster, R. Kneer, Proc. Combust. Inst. 33 (2011) 3407-3413 DOI 10.1016/j.proci.2010.05.047.

[35] C. K. Law, A. Makino, T. F. Lu, Combust. Flame 145 (4) (2006) 808-819 DOI 10.1016/j.combustflame.2006.01.009.